Auxiliary-boson and DMFT studies of bond ordering instabilities of t-J-V models on the square lattice

Auxiliary-boson and DMFT studies of bond ordering instabilities of t-J-V models on the square lattice

Andrea Allais, Johannes Bauer, and Subir Sachdev

Department of Physics, Harvard University, Cambridge MA 02138

(Dated: April 4, 2014)

Abstract

We examine the influence of strong on-site Coulomb interactions on instabilities of the metallic state on the square lattice to general forms of bond order. The Mott correlations are accounted for by the auxiliary-boson method, and by dynamical mean field theory calculations, complementing our recent work (arXiv:1402.4807) using Gutzwiller projected variational wavefunctions. By the present methods, we find that the on-site Mott correlations do not significantly modify the structure of the bond ordering instabilities which preserve time-reversal symmetry, but they do enhance the instability towards time-reversal symmetry breaking "staggered flux" states.

I. INTRODUCTION

In a recent paper[1], we examined instabilities of t-J-V models on the square lattice to arbitrary orderings in the spin-singlet, particle-hole channel, and accounted for the on-site Coulomb interactions by a variational wavefunction which projected out sites with double occupancy. In the present paper we will examine essentially the same models, but will account for the on-site interactions by the auxiliary-boson method (also called the "slave-boson" method) and dynamical mean field theory (DMFT) calculations. As in the previous work[1], our analysis allows for charged stripes,[2] checkerboard and bond density waves,[3–5] Ising-nematic order,[6–8] staggered flux states,[9–13] and states with spontaneous currents.[14]

In our works[1,15,16], ordering wavevectors associated with hot spots on the Fermi surface play a special role (see Fig. 1). In Section II, we will introduce the instabilities in the simpler

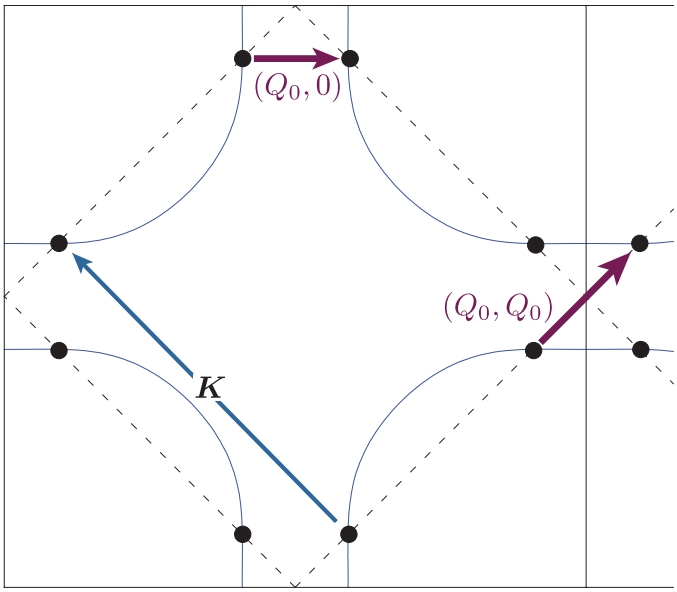

FIG. 1: Fermi surface with $t_1 = 1$, $t_2 = -0.32$, $t_3 = 0.128$, and $\mu = -1.11856$. For this dispersion we have $Q_0 = 4\pi/11$.

context of a 'generalized RPA' analysis of a model which includes an on-site repulsion, U, between the electrons. Our main results are in Section III, where we will take the limit $U \to \infty$ using the large N limit of a model with SU($2N$) spin rotation symmetry. In Section IV we perform an alternative calculation where the effective of large repulsion is included via a DMFT self-energy.

II. RPA ANALYSIS

This section will carry out a computation similar to that in Ref. 15, but we will work with a more general Hamiltonian and use a slightly different formalism. We consider electrons $c_{i\alpha}$ on the sites, i, of a square lattice, with $\alpha =\uparrow,\downarrow$ the spin index, and repeated spin indices, $\alpha, \beta \ldots$, are implicitly summed over. We work with the following Hamiltonian

$$\begin{aligned} H &= H_t + H_C + H_J \\ H_t &= -\sum_{i,j} t_{ij} c^\dagger_{i\alpha} c_{j\alpha} - \mu \sum_i c^\dagger_{i\alpha} c_{i\alpha} \\ H_C &= U \sum_i c^\dagger_{i\uparrow} c_{i\uparrow} c^\dagger_{i\downarrow} c_{i\downarrow} + \sum_{i<j} V_{ij} c^\dagger_{i\alpha} c_{i\alpha} c^\dagger_{j\beta} c_{j\beta} \\ H_J &= \sum_{i<j} \sum_a \frac{J_{ij}}{4} \sigma^a_{\alpha\beta} \sigma^a_{\gamma\delta} c^\dagger_{i\alpha} c_{i\beta} c^\dagger_{j\gamma} c_{j\delta}, \end{aligned} \tag{1}$$

where σ^a are the Pauli matrices with $a = x, y, z$. We will consider first, second, and third neighbor hopping t_1, t_2, t_3. Similarly, we have first, second, and third Coulomb and exchange interactions V_1, V_2, V_3 and J_1, J_2, and J_3.

We now introduce our generalized order parameters, $P_{\boldsymbol{Q}}(\boldsymbol{k})$, at wavevector $\boldsymbol{Q}$ in the particle-hole channel by the parameterization

$$\left\langle c^\dagger_{i\alpha} c_{j\alpha} \right\rangle = \sum_{\boldsymbol{Q}} \left[\int \frac{d^2k}{4\pi^2} P_{\boldsymbol{Q}}(\boldsymbol{k}) e^{i\boldsymbol{k}\cdot(\boldsymbol{r}_i - \boldsymbol{r}_j)} \right] e^{i\boldsymbol{Q}\cdot(\boldsymbol{r}_i + \boldsymbol{r}_j)/2}. \tag{2}$$

A conventional charge density wave at wavevector $\boldsymbol{Q}$ has $P_{\boldsymbol{Q}}(\boldsymbol{k})$ independent of $\boldsymbol{k}$ so that Eq. (2) is non-zero only for $i = j$. However, optimization of the bond energies requires that we allow $P_{\boldsymbol{Q}}(\boldsymbol{k})$ to be an arbitrary function of $\boldsymbol{k}$ in the first Brillouin zone. Here, we will find it useful to expand $P_{\boldsymbol{Q}}(\boldsymbol{k})$ in terms of a set of orthonormal basis functions $\phi_\ell(\boldsymbol{k})$

$$P_{\boldsymbol{Q}}(\boldsymbol{k}) = \sum_\ell \mathcal{P}_\ell(\boldsymbol{Q}) \phi_\ell(\boldsymbol{k}), \tag{3}$$

and the coefficients $\mathcal{P}_\ell(\boldsymbol{Q})$ become our order parameters. As we will shortly see, for the Hamiltonians we work with it is only necessary to include a finite set of values of ℓ in Eq. (3): we work with the 13 basis functions $\phi_\ell(\boldsymbol{k})$ as shown in Table I.

We take the index $\ell = 0, 1, \ldots 12$. Note that the orderings with $\ell = 0, \ldots 6$ represent charge/bond density waves which preserve time-reversal, while those with $\ell = 7, \ldots 12$ represent states with spontaneous currents which break time-reversal.

ℓ	$\phi_\ell(\boldsymbol{k})$	$\mathcal{J}_\ell$	$\mathcal{V}_\ell$	ℓ	$\phi_\ell(\boldsymbol{k})$	$\mathcal{J}_\ell$	$\mathcal{V}_\ell$
0	1	0	U				
1	$\cos k_x - \cos k_y$	J_1	V_1	7	$\sin k_x - \sin k_y$	J_1	V_1
2	$\cos k_x + \cos k_y$	J_1	V_1	8	$\sin k_x + \sin k_y$	J_1	V_1
3	$2\sin k_x \sin k_y$	J_2	V_2	9	$2\cos k_x \sin k_y$	J_2	V_2
4	$2\cos k_x \cos k_y$	J_2	V_2	10	$2\sin k_x \cos k_y$	J_2	V_2
5	$\cos(2k_x) - \cos(2k_y)$	J_3	V_3	11	$\sin(2k_x) - \sin(2k_y)$	J_3	V_3
6	$\cos(2k_x) + \cos(2k_y)$	J_3	V_3	12	$\sin(2k_x) + \sin(2k_y)$	J_3	V_3

TABLE I: Relevant basis functions

A key step is to rewrite the interaction terms Eq. (1) in the following form

$$H_J + H_C = \sum_{\boldsymbol{k},\boldsymbol{k}',\boldsymbol{q}} \sum_{\ell=0}^{12} \phi_\ell(\boldsymbol{k})\phi_\ell(\boldsymbol{k}') \left[\sum_a \frac{\mathcal{J}_\ell}{8} c^\dagger_{\boldsymbol{k}'-\boldsymbol{q}/2,\alpha}\, \sigma^a_{\alpha\beta}\, c_{\boldsymbol{k}-\boldsymbol{q}/2,\beta}\, c^\dagger_{\boldsymbol{k}+\boldsymbol{q}/2,\gamma}\, \sigma^a_{\gamma\delta}\, c_{\boldsymbol{k}'+\boldsymbol{q}/2,\delta} + \frac{\mathcal{V}_\ell}{2} c^\dagger_{\boldsymbol{k}'-\boldsymbol{q}/2,\alpha}\, c_{\boldsymbol{k}-\boldsymbol{q}/2,\alpha}\, c^\dagger_{\boldsymbol{k}+\boldsymbol{q}/2,\beta}\, c_{\boldsymbol{k}'+\boldsymbol{q}/2,\beta} \right] \tag{4}$$

where the $\phi_\ell(\boldsymbol{k})$ are 13 orthonormal basis functions in Table I, and $\mathcal{J}_\ell$ and $\mathcal{V}_\ell$ are the corresponding couplings shown in Table I. The appearance of a finite set of basis functions in Eq. (4) is the reason we are able to truncate the expansion in Eq. (3).

We can now use the basis $\phi_\ell(\boldsymbol{k})$ to also decompose the Bethe-Salpeter equation in the spin-singlet, particle-hole channel, as shown in Fig. 2. The eigenmodes of the resulting T-matrix $T_{\ell m}(\boldsymbol{Q})$ will determine the structure of the ordering, $\mathcal{P}_\ell(\boldsymbol{Q})$ at the wavevector $\boldsymbol{Q}$.

Summing ladder diagrams for both direct and exchange interactions we obtain

$$T_{\ell m}(\boldsymbol{Q}) = \left(\frac{3}{4}\mathcal{J}_\ell + \mathcal{V}_\ell\right)\delta_{\ell m} - 2\delta_{\ell,0}\delta_{m,0}W(\boldsymbol{Q}) + \frac{1}{2}\sum_{n=0}^{12}\left(\frac{3}{4}\mathcal{J}_\ell + \mathcal{V}_\ell\right)\Pi_{\ell n}(\boldsymbol{Q})T_{nm}(\boldsymbol{Q}) - \delta_{\ell,0}\sum_{n=0}^{12} W(\boldsymbol{Q})\Pi_{0n}(\boldsymbol{Q})T_{nm}(\boldsymbol{Q}) \tag{5}$$

where

$$W(\boldsymbol{Q}) \equiv \sum_{\ell=0}^{12} \mathcal{V}_\ell \phi_\ell(0)\phi_\ell(\boldsymbol{Q}) \tag{6}$$

is the direct interaction, and $\Pi_{\ell m}(\boldsymbol{Q})$ is a 13×13 matrix which is the polarizability of the Hamiltonian H_C

$$\Pi_{\ell m}(\boldsymbol{Q}) = 2\sum_{\boldsymbol{k}} \phi_\ell(\boldsymbol{k})\phi_m(\boldsymbol{k}) \frac{f(\varepsilon(\boldsymbol{k}-\boldsymbol{Q}/2)) - f(\varepsilon(\boldsymbol{k}+\boldsymbol{Q}/2))}{\varepsilon(\boldsymbol{k}+\boldsymbol{Q}/2) - \varepsilon(\boldsymbol{k}-\boldsymbol{Q}/2)} \tag{7}$$

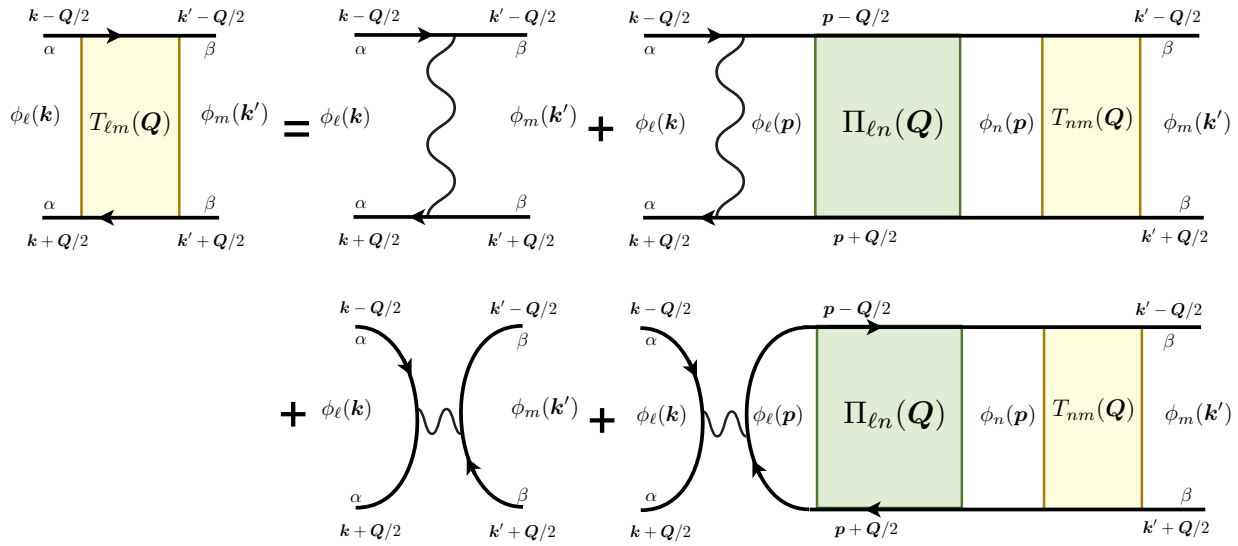

FIG. 2: Schematic equation for the T-matrix in the spin-singlet particle-hole channel with total momentum $\boldsymbol{Q}$

with $\varepsilon(\boldsymbol{k})$ is the single particle dispersion:

$$\varepsilon(\boldsymbol{k}) = -2t_1(\cos(k_x) + \cos(k_y)) - 4t_2\cos(k_x)\cos(k_y) - 2t_3(\cos(2k_x) + \cos(2k_y)) - \mu. \quad (8)$$

We choose the dispersion $\varepsilon(\boldsymbol{k})$ to have hot spots which intersect the magnetic Brillouin zone boundary, as shown in Fig. 1. The hot spots for this dispersion are separated by the vectors shown with $Q_0 = 4\pi/11$. Note that Q_0 is simply a geometric property of the Fermi surface, and plays no special role in the Hamiltonian.

By rearranging terms in Eq. (5), we see that the charge-ordering instability is determined by the lowest eigenvalues, $\lambda_{\boldsymbol{Q}}$ of the matrix

$$\delta_{\ell m} - \frac{1}{2}\left(\frac{3}{4}\mathcal{J}_\ell + \mathcal{V}_\ell\right)\Pi_{\ell m}(\boldsymbol{Q}) + \delta_{\ell,0}W(\boldsymbol{Q})\Pi_{0m}(\boldsymbol{Q}), \quad (9)$$

and the $\mathcal{P}_m(\boldsymbol{Q})$ are determined by the corresponding right eigenvector. The values of $\lambda_{\boldsymbol{Q}}$ are shown in Figs. 3 and 4 for the metallic state with the Fermi surface in Fig. 1.

In Fig. 3 we consider a case with vanishing on-site interactions, as in Ref. 15. As found previously, the lowest eigenvalue is at $\boldsymbol{Q} \approx (Q_0, Q_0)$ and the corresponding eigenvector is purely d-wave.

We turn on Coulomb interactions in Fig. 4, while keeping other parameters the same. The main change is that the eigenvalues near $\boldsymbol{Q} = (\pi, \pi)$ become significantly smaller. The

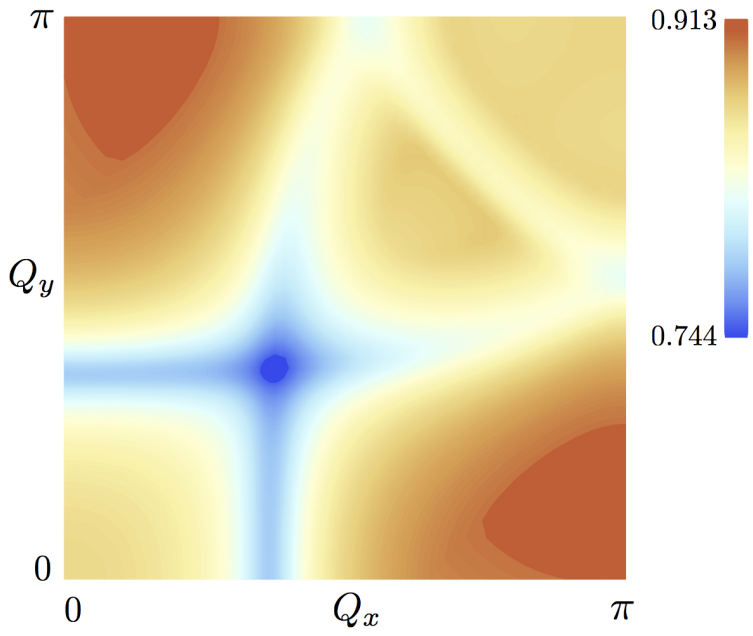

FIG. 3: Lowest eigenvalues, $\lambda_{\boldsymbol{Q}}$, of the 13×13 matrix in Eq. (9) at a temperature $T = 0.06$. The Fermi surface is as in Fig. 1, and the interaction couplings are $J_1 = 0.5$, $J_2 = 0.2$, $J_3 = 0.05$, $U = 0$, $V_1 = 0$, $V_2 = 0$, $V_3 = 0$. Minimized over $\boldsymbol{Q}$, the lowest eigenvalue is at $\boldsymbol{Q} = (0.38, 0.38)\pi$; this is very close to the value $Q_0 = 0.36\pi$ as determined from the Fermi surface in Fig. 1. The eigenvector at $\boldsymbol{Q} = (0.38, 0.38)\pi$ is $P_{\boldsymbol{Q}}(\boldsymbol{k}) = 0.9996(\cos(k_x) - \cos(k_y)) + 0.0275(\cos(2k_x) - \cos(2k_y))$.

eigenvectors in this region of $\boldsymbol{Q}$ break time-reversal[15], and the eigenvector at $\boldsymbol{Q} = (\pi, \pi)$ is $P_{\boldsymbol{Q}}(\boldsymbol{k}) = \sin(k_x) - \sin(k_y)$. Some intuition about which wavevector is favored with the corresponding eigenvector can be gained from the plots of the relevant integrand in the instability equation.

$$\Pi(\boldsymbol{k}, \boldsymbol{Q}) = \frac{f(\varepsilon(\boldsymbol{k} - \boldsymbol{Q}/2)) - f(\varepsilon(\boldsymbol{k} + \boldsymbol{Q}/2))}{\varepsilon(\boldsymbol{k} + \boldsymbol{Q}/2) - \varepsilon(\boldsymbol{k} - \boldsymbol{Q}/2)} \tag{10}$$

in Fig. 5.

In both Figs. 3 and 4, there is a ridge of minima extending from (Q_0, Q_0) to $(0, Q_0)$, and also to $(Q_0, 0)$. The latter wavevectors are close to the experimentally observed values.[17] At the wavevector $\boldsymbol{Q} = (0, Q_0)$, the charge ordering eigenvector for Fig. 4 is

$$\begin{aligned} P_{\boldsymbol{Q}}(\boldsymbol{k}) \;=\; & -0.352 - 0.931\big[\cos(k_x) - \cos(k_y)\big] + 0.017\big[\cos(k_x) + \cos(k_y)\big] \\ & -\; 0.168\cos(k_x)\cos(k_y) - 0.028\big[\cos(2k_x) - \cos(2k_y)\big] + 0.029\big[\cos(2k_x) + \cos(2k_y)\big]. \end{aligned} \tag{11}$$

So the largest component at this $\boldsymbol{Q}$ remains a d-wave on the nearest neighbor bonds, but

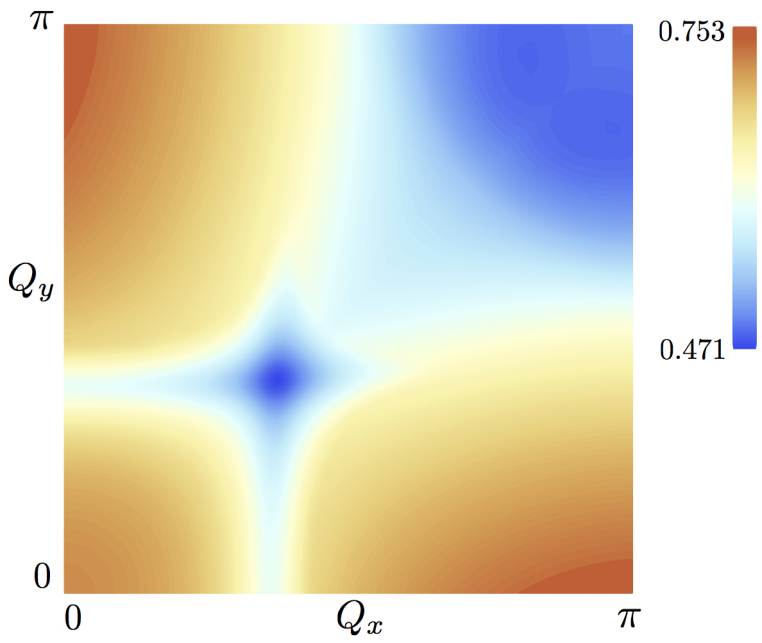

FIG. 4: As in Fig. 3, with all parameters the same apart from $U = 1$, $V_1 = 0.4$, $V_2 = 0.2$, and $V_3 = 0.05$. Minimized over $\boldsymbol{Q}$, the lowest eigenvalue is again at $\boldsymbol{Q} = (0.38, 0.38)\pi$ and the corresponding eigenvector is $P_{\boldsymbol{Q}}(\boldsymbol{k}) = 0.9995(\cos(k_x) - \cos(k_y)) + 0.0312(\cos(2k_x) - \cos(2k_y))$. Now there are also small, but slightly larger, eigenvalues near $\boldsymbol{Q} = (\pi, \pi)$ with eigenvectors which break time-reversal.

now there is a significant on-site density wave.

There is also a local minimum in Fig. 4 at $\boldsymbol{Q} = (\pi, \pi)$. Here the eigenvector is

$$P_{\boldsymbol{Q}}(\boldsymbol{k}) = \sin(k_x) - \sin(k_y). \tag{12}$$

This represents the "staggered flux" state of Refs. 9–13. This state was called a "d-density wave" in Ref. 11, which is an unfortunate terminology from our perspective. With our identification of the bond expectation values in Eq. (2), this state is actually a p-density wave,[15] as is evident from Eq. (12).

III. $U \to \infty$ LIMIT

We will continue to work with the Hamiltonian in Eq. (1), but will now set $U = \infty$. The $U = \infty$ constraint is implemented by the auxiliary-boson decomposition

$$c_{i\alpha} = b_i^\dagger f_{i\alpha} \tag{13}$$

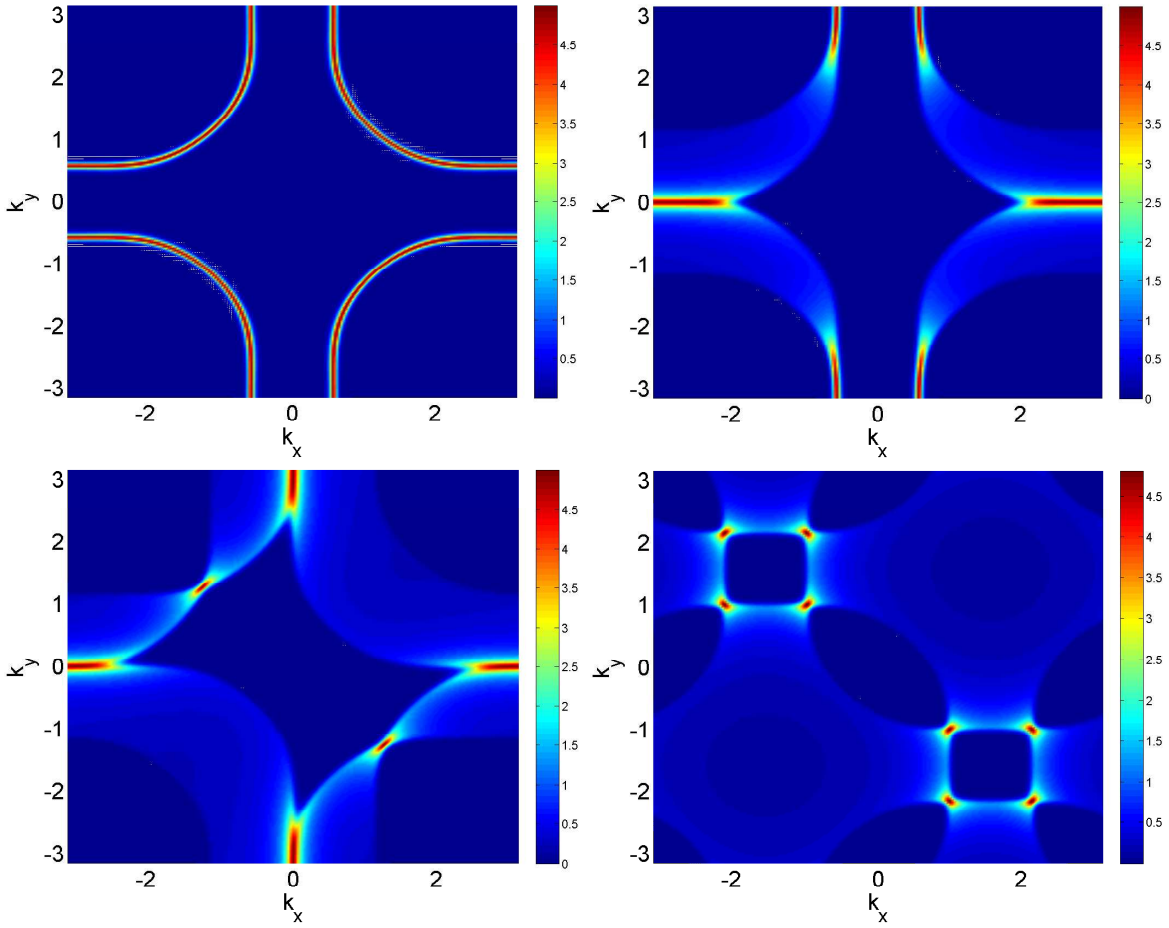

FIG. 5: Color plots of the magnitude of the integrand $\Pi(\boldsymbol{k}, \boldsymbol{Q})$ in Eq. (10) for $T = 0.05$ and hopping parameters as before as function of $\boldsymbol{k}$ for different $\boldsymbol{Q} = 0$, $Q_0(1,0)$, $Q_0(1,1)$, (π,π) (from top left to bottom right). The result for $\boldsymbol{Q} = 0$ is strongly peaked at the Fermi surface. We see that for $\boldsymbol{Q} = Q_0(1,0), Q_0(1,1)$ we obtain large matrix elements $\Pi_{11}(\boldsymbol{Q})$ with d-wave symmetry $\phi_1(\boldsymbol{k})$ as $\phi_1(\boldsymbol{k})^2$ is peaked at $\pm(\pi,0)$, $\pm(0,\pi)$. For $\boldsymbol{Q} = (\pi,\pi)$ the largest contribution is for $\Pi_{77}(\boldsymbol{Q})$ with the $\phi_7(\boldsymbol{k})$ eigenfunction where $\phi_7(\boldsymbol{k})^2$ is peaked at $\pm(-\pi/2, \pi/2)$.

where b_i is a canonical boson and $f_{i\alpha}$ is a canonical fermion, along with the constraint

$$b_i^\dagger b_i + f_{i\alpha}^\dagger f_{i\alpha} = N. \tag{14}$$

Here we allow the index $\alpha = 1 \ldots 2N$, so that the model has SU($2N$) symmetry. The constraint can then be systematically implemented in the large N limit.[9,18]

We can write the SU($2N$) Lagrangian as

$$\begin{aligned}\mathcal{L} \;=\; & \sum_i \left[f_{i\alpha}^\dagger \left(\frac{\partial}{\partial \tau} - \mu + i\lambda_i \right) f_{i\alpha} + b_i^\dagger \left(\frac{\partial}{\partial \tau} + i\lambda_i \right) b_i - iN\lambda_i \right] \\ & -\frac{1}{N} \sum_{i,j} t_{ij}^0 b_i b_j^\dagger f_{i\alpha}^\dagger f_{j\alpha} + \frac{1}{N} \sum_{i<j} V_{ij} (N - b_i^\dagger b_i)(N - b_j^\dagger b_j) \\ & + \sum_{i<j} J_{ij} \left(2N|P_{ij}|^2 - P_{ij}^* f_{i\alpha}^\dagger f_{j\alpha} - P_{ij} f_{j\alpha}^\dagger f_{i\alpha} \right) \end{aligned} \tag{15}$$

where we have decoupled the exchange interaction by a Hubbard-Stratanovich variable P_{ij} residing on the bonds, and absorbed a contribution of $-J_{ij}/4$ into the definition of V_{ij}. Also, we have written the fermion hopping as t^0 because this will undergo a renormalization before determining the fermion dispersion.

A. $N = \infty$ theory

We take $b_i = \sqrt{N}\,\overline{b}$, $\lambda_i = -i\overline{\lambda}$ and $P_{ij} = \overline{P}_{1,2,3}$ for ij first, second, third neighbors. Then the fermion dispersion is

$$H_f = \sum_{\boldsymbol{k}} E(\boldsymbol{k}) f_{\boldsymbol{k}\alpha}^\dagger f_{\boldsymbol{k}\alpha} \tag{16}$$

with

$$E(\boldsymbol{k}) = -\overline{b}^2 \gamma(\boldsymbol{k}) - \gamma_J(\boldsymbol{k}) - \mu + \overline{\lambda}, \tag{17}$$

where

$$\gamma(\boldsymbol{k}) = 2t_1^0(\cos(k_x) + \cos(k_y)) + 4t_2^0 \cos(k_x)\cos(k_y) + 2t_3^0(\cos(2k_x) + \cos(2k_y)), \tag{18}$$

and

$$\gamma_J(\boldsymbol{k}) = 2J_1P_1(\cos(k_x) + \cos(k_y)) + 4J_2P_2 \cos(k_x)\cos(k_y) + 2J_3P_3(\cos(2k_x) + \cos(2k_y)). \tag{19}$$

From these relations we see that the renormalized fermion hopping parameters are

$$t_i = t_i^0 \overline{b}^2 + J_i P_i, \tag{20}$$

where $i = 1, 2, 3$.

The mean-field equations for the P's are obtained from the $N = \infty$ saddle point condition, which yield

$$\begin{aligned} P_1 &= \sum_{\boldsymbol{k}} \cos(k_x)\, f(E(\boldsymbol{k})) \\ P_2 &= \sum_{\boldsymbol{k}} \cos(k_x + k_y)\, f(E(\boldsymbol{k})) \\ P_3 &= \sum_{\boldsymbol{k}} \cos(2k_x)\, f(E(\boldsymbol{k})). \end{aligned} \tag{21}$$

The constraint equation from the saddle point of λ_i is

$$\bar{b}^2 = 1 - 2\sum_{\boldsymbol{k}} f(E(\boldsymbol{k})). \tag{22}$$

And finally, the saddle point equation for $\bar{b}$ is

$$\overline{\lambda} = 4(V_1 + V_2 + V_3)(1 - \bar{b}^2) + 2\sum_{\boldsymbol{k}} \gamma(\boldsymbol{k}) f(E(\boldsymbol{k})). \tag{23}$$

B. $1/N$ fluctuations

It is useful to manipulate the exchange interactions into the following form

$$\begin{aligned} H_J &= -\sum_{i,j} \frac{J_{ij}}{4N} f^\dagger_{i\alpha} f_{j\alpha} f^\dagger_{j\beta} f_{i\beta} \\ &= -\frac{1}{4N} \sum_{\boldsymbol{k},\boldsymbol{k}',\boldsymbol{Q}} \left(\sum_a J_{i,i+a} e^{i(\boldsymbol{k}-\boldsymbol{k}')\cdot\boldsymbol{a}} \right) f^\dagger_{\boldsymbol{k}+\boldsymbol{Q}/2,\alpha} f_{\boldsymbol{k}-\boldsymbol{Q}/2,\alpha} f^\dagger_{\boldsymbol{k}'-\boldsymbol{Q}/2,\beta} f_{\boldsymbol{k}'-\boldsymbol{Q}/2,\beta} \\ &= -\frac{1}{4N} \sum_{\boldsymbol{Q}} \sum_{\ell=1}^{12} \mathcal{J}_\ell \left| \sum_{\boldsymbol{k}} \phi_\ell(\boldsymbol{k}) f^\dagger_{\boldsymbol{k}+\boldsymbol{Q}/2,\alpha} f_{\boldsymbol{k}-\boldsymbol{Q}/2,\alpha} \right|^2, \end{aligned} \tag{24}$$

where a extends over first, second, and third neighbors, and the $\mathcal{J}_\ell$ and the ϕ_ℓ are the same as in Table I. Note that in this section the index ℓ extends from $\ell = 1$ to $\ell = 12$ (implicitly, where not noted), and the $\ell = 0$ basis states in Table I are not included. Now we can decouple the exchange coupling to

$$H_J = \sum_{\boldsymbol{Q}} \sum_{\ell=1}^{12} \mathcal{J}_\ell \left[N|\mathcal{P}_\ell(\boldsymbol{Q})|^2 - \sum_{\boldsymbol{k}} \mathcal{P}_\ell(-\boldsymbol{Q}) \phi_\ell(\boldsymbol{k}) f^\dagger_{\boldsymbol{k}+\boldsymbol{Q}/2,\alpha} f_{\boldsymbol{k}-\boldsymbol{Q}/2,\alpha} \right], \tag{25}$$

with $\mathcal{P}_\ell(-\boldsymbol{Q}) = \mathcal{P}^*_\ell(\boldsymbol{Q})$. We can now see that the $\mathcal{P}_\ell(\boldsymbol{Q})$ are similar to the order parameters as those introduced in Eq. (3), but they now refer to the fermions f_α rather than the electrons

c_α. These differ by a factor of $\bar{b}$ in the large N limit, and so the corresponding $\mathcal{P}_\ell(\boldsymbol{Q})$ differ by a factor of $\bar{b}^2$. The mean-field values of the $\mathcal{P}_\ell(\boldsymbol{Q})$ are

$$\overline{\mathcal{P}_\ell}(\boldsymbol{Q}) = \delta_{\boldsymbol{Q},0}\,\{0, 2P_1, 0, 2P_2, 0, 2P_3, 0, 0, 0, 0, 0, 0\}. \tag{26}$$

For the fluctuations about mean-field, we fix the unitary gauge, and work at zero frequency of all bosonic fields. Then we can parameterize the fluctuations as

$$\mathcal{P}_\ell(\boldsymbol{Q}) \;=\; \overline{\mathcal{P}_\ell}(\boldsymbol{Q}) + \frac{1}{\sqrt{\mathcal{J}_\ell}} p_\ell(\boldsymbol{Q}), \tag{27}$$

$$\lambda_i \;=\; -i\overline{\lambda} + \sum_{\boldsymbol{Q}} \lambda(\boldsymbol{Q}) e^{i\boldsymbol{Q}\cdot\boldsymbol{r}_i}, \tag{28}$$

$$b_i \;=\; \sqrt{N}\,\bar{b} + \sqrt{N}\sum_{\boldsymbol{Q}} b(\boldsymbol{Q}) e^{i\boldsymbol{Q}\cdot\boldsymbol{r}_i}, \tag{29}$$

where $\lambda(-\boldsymbol{Q}) = \lambda^*(\boldsymbol{Q})$, $b(-\boldsymbol{Q}) = b^*(\boldsymbol{Q})$, $p_\ell(-\boldsymbol{Q}) = p_\ell^*(\boldsymbol{Q})$. Then the Lagrangian (15) can be written as

$$\begin{aligned}
\mathcal{L} \;=\; & \mathcal{L}_0 + N\sum_{\boldsymbol{Q}}\Bigg[\sum_\ell |p_\ell(\boldsymbol{Q})|^2 + 2i\bar{b}\sum_{\boldsymbol{Q}}\lambda(\boldsymbol{Q})b(-\boldsymbol{Q}) \\
& + \left[\overline{\lambda} + 4(V_1+V_2+V_3)(\bar{b}^2-1) + 2\bar{b}^2\gamma_V(\boldsymbol{Q})\right] b(\boldsymbol{Q})b(-\boldsymbol{Q})\Bigg] \\
& + \sum_{\boldsymbol{k}} f^\dagger_{\boldsymbol{k}\alpha}\left(\frac{\partial}{\partial\tau} + E(\boldsymbol{k})\right) f_{\boldsymbol{k}\alpha} - \bar{b}\sum_{\boldsymbol{k},\boldsymbol{Q}}\left[\gamma(\boldsymbol{k}-\boldsymbol{Q}/2) + \gamma(\boldsymbol{k}+\boldsymbol{Q}/2)\right] b(\boldsymbol{Q}) f^\dagger_{\boldsymbol{k}+\boldsymbol{Q}/2,\alpha} f_{\boldsymbol{k}-\boldsymbol{Q}/2,\alpha} \\
& - \sum_{\boldsymbol{k},\boldsymbol{Q}_1,\boldsymbol{Q}_2}\gamma(\boldsymbol{k})b(\boldsymbol{Q}_1)b(\boldsymbol{Q}_2) f^\dagger_{\boldsymbol{k}+\boldsymbol{Q}_1,\alpha} f_{\boldsymbol{k}-\boldsymbol{Q}_2,\alpha} + \sum_{\boldsymbol{k},\boldsymbol{Q}}\left[i\lambda(\boldsymbol{Q}) - \sqrt{\mathcal{J}_\ell}\, p_\ell(-\boldsymbol{Q})\,\phi_\ell(\boldsymbol{k})\right] f^\dagger_{\boldsymbol{k}+\boldsymbol{Q}/2,\alpha} f_{\boldsymbol{k}-\boldsymbol{Q}/2,\alpha},
\end{aligned} \tag{30}$$

where

$$\gamma_V(\boldsymbol{k}) = 2V_1(\cos(k_x)+\cos(k_y)) + 4V_2\cos(k_x)\cos(k_y) + 2V_3(\cos(2k_x)+\cos(2k_y)). \tag{31}$$

We integrate out the fermions and obtain

$$\mathcal{L} = \mathcal{L}_0 + \frac{N}{2}\sum_{\boldsymbol{Q}}\Bigg[(p_\ell(-\boldsymbol{Q}), b(-\boldsymbol{Q}), \lambda(-\boldsymbol{Q}))\begin{pmatrix} 2\delta_{\ell m} - \sqrt{\mathcal{J}_\ell\mathcal{J}_m}\,\Pi_{\ell m}(\boldsymbol{Q}) & K_{4\ell}(\boldsymbol{Q}) & K_{5\ell}(\boldsymbol{Q}) \\ K_{4m}(\boldsymbol{Q}) & K_1(\boldsymbol{Q}) & K_2(\boldsymbol{Q}) \\ K_{5m}(\boldsymbol{Q}) & K_2(\boldsymbol{Q}) & K_3(\boldsymbol{Q}) \end{pmatrix}\begin{pmatrix} p_m(\boldsymbol{Q}) \\ b(\boldsymbol{Q}) \\ \lambda(\boldsymbol{Q}) \end{pmatrix}, \tag{32}$$

where

$$
\begin{aligned}
K_1(\boldsymbol{Q}) &= 2\overline{\lambda} + 8(V_1+V_2+V_3)(\overline{b}^2-1) + 4\overline{b}^2\gamma_V(\boldsymbol{k}), \\
&\quad + \sum_{\boldsymbol{k}} \left[-4\gamma(\boldsymbol{k}) f(E(\boldsymbol{k}+\boldsymbol{Q})) - \overline{b}^2 \left[\gamma(\boldsymbol{k}-\boldsymbol{Q}/2)+\gamma(\boldsymbol{k}+\boldsymbol{Q}/2)\right]^2 \Pi(\boldsymbol{k},\boldsymbol{Q}) \right], \\
K_2(\boldsymbol{Q}) &= 2i\overline{b} + i\overline{b} \sum_{\boldsymbol{k}} \left[\gamma(\boldsymbol{k}-\boldsymbol{Q}/2)+\gamma(\boldsymbol{k}+\boldsymbol{Q}/2)\right] \Pi(\boldsymbol{k},\boldsymbol{Q}), \\
K_3(\boldsymbol{Q}) &= \sum_{\boldsymbol{k}} \Pi(\boldsymbol{k},\boldsymbol{Q}), \\
K_{4\ell}(\boldsymbol{Q}) &= -\overline{b}\sqrt{\mathcal{J}_\ell} \sum_{\boldsymbol{k}} \phi_\ell(\boldsymbol{k}) \left[\gamma(\boldsymbol{k}-\boldsymbol{Q}/2)+\gamma(\boldsymbol{k}+\boldsymbol{Q}/2)\right] \Pi(\boldsymbol{k},\boldsymbol{Q}), \\
K_{5\ell}(\boldsymbol{Q}) &= i\sqrt{\mathcal{J}_\ell} \sum_{\boldsymbol{k}} \phi_\ell(\boldsymbol{k}) \Pi(\boldsymbol{k},\boldsymbol{Q}),
\end{aligned}
\tag{33}
$$

with

$$
\Pi(\boldsymbol{k},\boldsymbol{Q}) = 2\frac{f(E(\boldsymbol{k}-\boldsymbol{Q}/2)) - f(E(\boldsymbol{k}+\boldsymbol{Q}/2))}{E(\boldsymbol{k}+\boldsymbol{Q}/2)) - E(\boldsymbol{k}-\boldsymbol{Q}/2)}, \tag{34}
$$

and $\Pi_{\ell m}(\boldsymbol{Q})$ defined as in Eq. (7).

We now perform the Gaussian integrals over the fields $\lambda(\boldsymbol{Q})$ and $b(\boldsymbol{Q})$, and then diagonalize the resulting quadratic form for the fields $p_\ell(\boldsymbol{Q})$. This step is the analog of our solution of the Bethe-Salpeter equation in Section II. Note that the quadratic form for the $p_\ell(\boldsymbol{Q})$ in Eq. (32) begins with a $2\delta_{\ell m}$, which is to be compared with the $\delta_{\ell m}$ in Eq. (9); consequently, the present eigenvalues $\lambda_{\boldsymbol{Q}}$ are to be compared with *twice* the eigenvalues in Section II. We also note that a related computation was carried out in a different gauge in the early work of Ref. 19, but they did not consider Fermi surfaces with hot spots.

Our results for the $\lambda_{\boldsymbol{Q}}$ are shown in Fig. 6, with the same set of parameters as in Fig. 4 in Section II but with the $U = \infty$ limit taken in the large N method. The results are very similar, but the eigenvalues of the time-reversal symmetry breaking 'staggered flux' state near $\boldsymbol{Q} = (\pi, \pi)$ are a bit larger now. The global minimum of $\lambda_{\boldsymbol{Q}}$ remains at $\boldsymbol{Q} = (0.38, 0.38)\pi$ and the corresponding eigenvector is purely d wave (note that the values of ℓ extend over $1 \ldots 12$):

$$
p_\ell(\boldsymbol{Q}) = \{0.996,\ 0,\ 0,\ 0,\ 0.087,\ 0,\ 0,\ 0,\ 0,\ 0,\ 0,\ 0\} \quad , \quad \boldsymbol{Q} = (0.38, 0.38)\pi\,. \tag{35}
$$

For the local minimum at $\boldsymbol{Q} = (0, 0.38)\pi$ the eigenvector is a mixture of s and d wave, as in Eq. (11):

$$
p_\ell(\boldsymbol{Q}) = \{0.988,\ 0.001,\ 0,\ 0.112,\ 0.077,\ -0.079, 0,\ 0,\ 0,\ 0,\ 0,\ 0\} \quad , \quad \boldsymbol{Q} = (0, 0.38)\pi\,. \tag{36}
$$

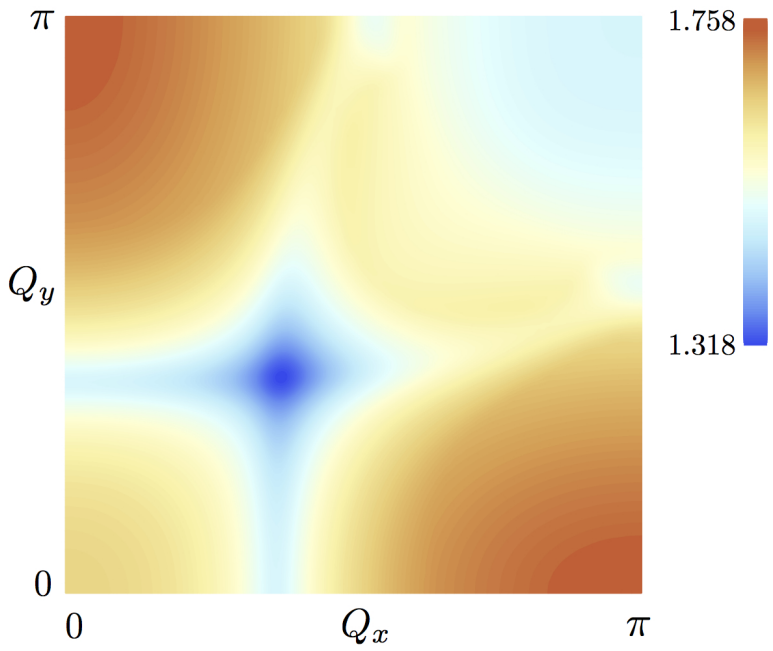

FIG. 6: As in Fig. 4, with all parameters the same apart from the $U = \infty$ limit taken via the auxiliary-boson method. As noted in the text, the present eigenvalues have to be compared with twice the eigenvalues in Fig. 4. The structure of the eigenvalues and eigenvectors is very similar to Fig. 4, with the main difference that the strength of the sub-dominant instability to the time-reversal symmetry breaking staggered flux state near (π, π) is now weaker.

For completeness, we present in Fig. 7 the auxiliary-boson results for precisely the same parameters used in Ref. 1 for the Gutzwiller projected variational wavefunctions. In moving from (a) to (c), we find increasing preference for the (Q_0, Q_0) instability, as in Ref. 1. However, in (a) the global eigenvalue minimum is for the staggered flux state at (π, π), while in Ref. 1 is was for the experimentally observed $(Q_0, 0)$ state. Ref. 1 had the staggered flux state preferred in (b), while here we find that charge order at (Q_0, Q_0) is preferred.

IV. DMFT APPROACH FOR LARGE U

In this section we present results of an alternative approach to describe the strong local repulsion. We first perform a dynamical mean field (DMFT) calculation[20] for the tight-binding model with dispersion $\varepsilon_{\boldsymbol{k}}$ for a certain filling factor and value of the interaction U. We use the resulting $\boldsymbol{k}$-independent self-energy $\Sigma(i\omega_n)$ to compute the instability matrix [cf.

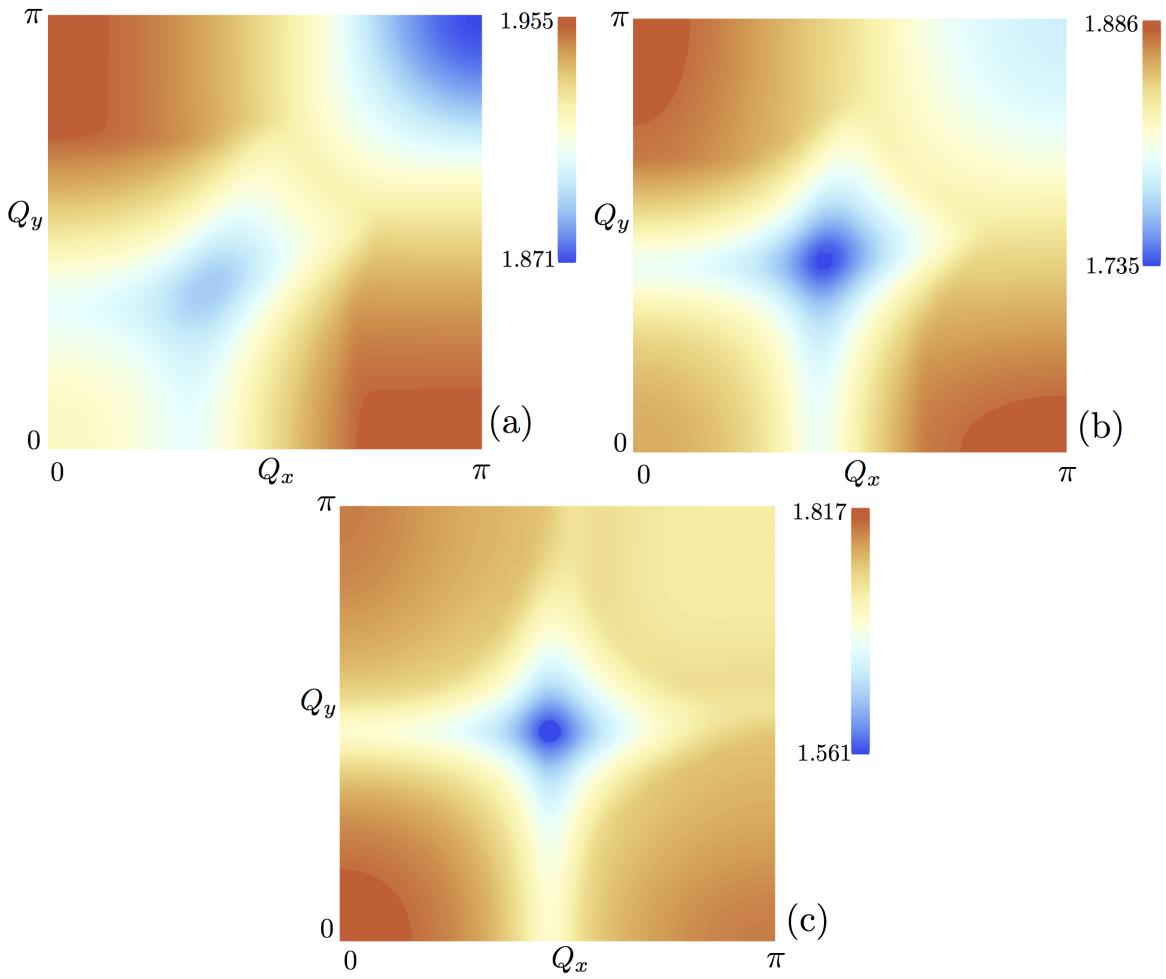

FIG. 7: As in Fig. 6, with the $U = \infty$ limit taken via the auxiliary-boson method. The parameters for the three figures are the same as those in Ref. 1: we have $t_1 = 1$, $t_2 \in \{0.5, 0.16, 0.18\}$, $t_3 \in \{0.6, 0.9, 1.6\}$, $J_1 \in \{0.09, 0.235, 0.4\}$, $V_1 \in \{1., 1.5, 0.5\}$, $J_2 = J_3 = V_2 = V_3 = 0$. The hole density in all three figures is 0.1, corresponding to $\mu \in \{-0.5256, -0.90285, -1.1174\}$.

Eq. (7)] related to the J-interaction,

$$\Pi_{\mathrm{DMFT},m,n}(\boldsymbol{Q}) = \sum_{\boldsymbol{k}} \phi_n(\boldsymbol{k}) \Pi_{\mathrm{DMFT}}(\boldsymbol{k}, \boldsymbol{Q}) \phi_m(\boldsymbol{k}), \tag{37}$$

where

$$\begin{aligned} \Pi_{\mathrm{DMFT}}(\boldsymbol{k}, \boldsymbol{Q}) &= -\frac{1}{\beta} \sum_n G(i\omega_n, \boldsymbol{k} + \boldsymbol{Q}/2) G(i\omega_n, \boldsymbol{k} - \boldsymbol{Q}/2) \\ &= -\frac{1}{\beta} \sum_n \frac{1}{i\omega_n - \varepsilon_{\boldsymbol{k}+\boldsymbol{Q}/2} + \mu - \Sigma(i\omega_n)} \frac{1}{i\omega_n - \varepsilon_{\boldsymbol{k}-\boldsymbol{Q}/2} + \mu - \Sigma(i\omega_n)}. \end{aligned}$$

This can be used to anlyze the instability in an equation analogous to Eq. (5). Such a calculation leads a renormalization of the low energy dispersion by a renormalization factor

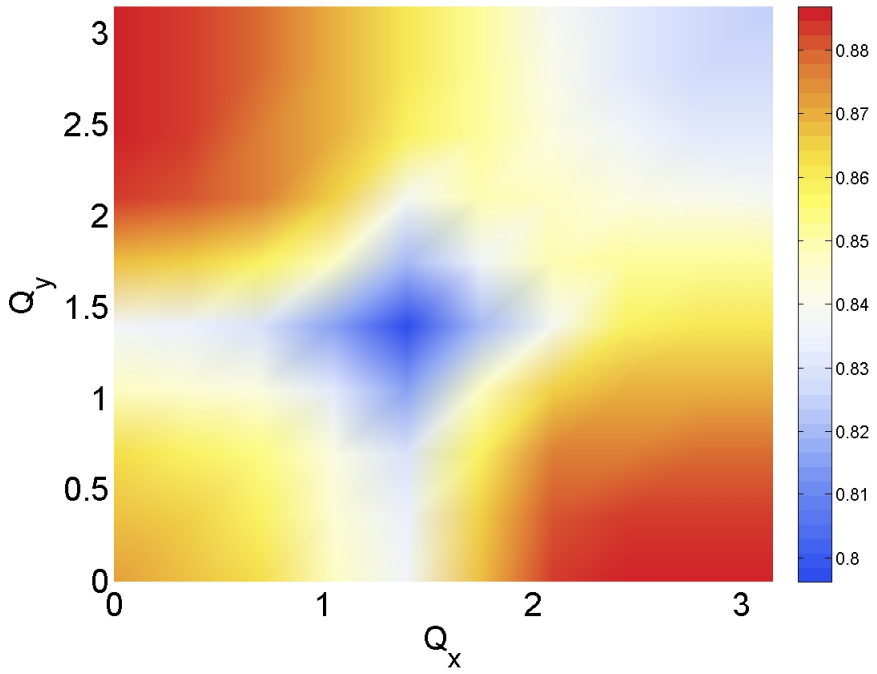

FIG. 8: Plot of the lowest eigenvalues $\lambda_{\boldsymbol{Q}}$ of the instability equation for different $\boldsymbol{Q}$. The parameters are $T = 0.01$, $n = 0.85$, $U = 8t_1^0$, $V_i = 0$ and the hopping parameters as before in Fig. 1. The structure of the eigenvalues and eigenvectors is very similar to Fig. 6.

$z = [1 - \mathrm{Re}\Sigma'(0)]^{-1}$, $\tilde{t}_i = zt_i^0$, similar to the auxiliary-boson calculation. It additionally accounts for damping effects of the excitations away from the Fermi surface and a split into low energy dispersion and Hubbard bands. In order to project out double occupancy completely, one should perform the DMFT calculation at $U \to \infty$. However, this leads to very small renormalization factors z,[24] at odds with experimental observations.[22,23] We therefore prefer to perform the calculation for values of $U \sim 1 - 1.5W$, where W is the bandwidth of the tight-binding model. Double occupancy is reduced to less than 0.05 in such calculations. There is no problem of double counting in this procedure since the J-interaction is absent in paramagnetic DMFT calculations.[20] The DMFT self-consistency problem is solved with the numerical renormalization group[21] at low temperature. The result of such a calculation for $J_1 = 0.5$ and filling factor $n = 0.85$ are displayed in Fig. 8.

As before the dominant instability is at (Q_0, Q_0) with subdominant instabilities at $(Q_0, 0)$ and (π, π), and the eigenfunctions are as discussed above. The value of $Q_0 \simeq 0.44\pi$ is a bit larger than what is expected from the Fermi surface geometry (see Fig. 1), where for the

parameters $Q_0 \simeq 0.39\pi$. We have restricted the analysis here to only finite J_1 such that the relevant basis functions are $\phi_n(\boldsymbol{k})$ with $n = 1, 2, 7, 8$. Note that the strength of the instability is reduced by the renormalization factor $z \simeq 0.25$ which also acts like a quasipartice weight. For other filling factors and interactions $U \sim 1.5W$ we find similar results as in Fig. 8. It is worth noting that at higher temperatures the global minimum can shift to (π, π). We conclude that the structure of dominant charge/bond ordering instabilities obtained from treating Mott correlations with DMFT is very similar to the results in Section III.

V. CONCLUSIONS

Our main conclusion is that Mott correlations, as implied by the auxiliary-boson and DMFT methods, do not significantly modify the conclusions of Ref. 15. As long as the metallic state has "hot spots" on its Fermi surface, its dominant instability in the spin-singlet, particle-hole channel is towards a bond-ordered state near wavevectors $(\pm Q_0, \pm Q_0)$ with a local d-wave symmetry of bond ordering; such a state has also been called an "incommensurate nematic". However, our present computations do show an enhanced instability towards a time-reversal symmetry breaking state with spontaneous currents: the "staggered flux" state.

The experimentally observed charge ordering at $(\pm Q_0, 0)$ and $(0, \pm Q_0)$ remained subdominant to ordering at $(\pm Q_0, \pm Q_0)$. Nevertheless, our computations do predict a predominantly d-wave form for the order parameter $P_{\boldsymbol{Q}}(\boldsymbol{k})$ at $\boldsymbol{Q} = (\pm Q_0, 0)$ and $(0, \pm Q_0)$, as shown in Eqs. (11) and (36). We note the variational computations in Ref. 1, using a wavefunction with double occupancy projected out, did find a regime in which the dominant charge ordering was at $(\pm Q_0, 0)$ and $(0, \pm Q_0)$. Other mechanisms for selecting the observed wavevector have also been proposed.[25,26]

Finally, we mention two recent experimental reports[27,28] concluding that the charge order at $(Q_0, 0)$ is predominantly d-wave, *i.e.* the $\ell = 1$ coefficient of the basis functions $\phi_\ell(\boldsymbol{k})$ in Table I is significantly larger than all other ℓ. This is just as in Eqs. (11) and (36).

Acknowledgments

We thank D. Chowdhury, A. Georges, and J. Sau for valuable discussions. The research was supported by the U.S. National Science Foundation under grant DMR-1103860, and by the Templeton Foundation. JB acknowledges financial support from the DFG through grant number BA 4371/1-1.

---

[1] A. Allais, J. Bauer, and S. Sachdev, arXiv:1402.4807.

[2] S. A. Kivelson, I. P. Bindloss, E. Fradkin, V. Oganesyan, J. M. Tranquada, A. Kapitulnik, and C. Howald, Rev. Mod. Phys. **75**, 1201 (2003).

[3] S. Sachdev, Rev. Mod. Phys. **75**, 913 (2003).

[4] M. Vojta and O. Rösch, Phys. Rev. B **77**, 094504 (2008).

[5] J. C. Séamus Davis and Dung-Hai Lee, Proc. Natl. Acad. Sci. **110**, 17623 (2013).

[6] H. Yamase and H. Kohno, J. Phys. Soc. Jpn. **69**, 2151 (2000).

[7] C. J. Halboth and W. Metzner, Phys. Rev. Lett. **85**, 5162 (2000).

[8] V. Oganesyan, S. A. Kivelson, and E. Fradkin, Phys. Rev. B **64**, 195109 (2001).

[9] I. Affleck and J. B. Marston, Phys. Rev. B **37**, 3774 (1988).

[10] Z. Wang, G. Kotliar, and X.-F. Wang, Phys. Rev. B **42**, 8690 (1990).

[11] S. Chakravarty, R. B. Laughlin, D. K. Morr, and C. Nayak, Phys. Rev. B **63**, 094503 (2001).

[12] P. A. Lee, N. Nagaosa, and X.-G. Wen, Rev. Mod. Phys. **78**, 17 (2006).

[13] R. B. Laughlin, Phys. Rev. B **89**, 035134 (2014).

[14] M. E. Simon and C. M. Varma, Phys. Rev. Lett. **89**, 247003 (2002).

[15] S. Sachdev and R. La Placa, Phys. Rev. Lett. **111**, 027202 (2013).

[16] J. D. Sau and S. Sachdev, Phys. Rev. B **89**, 075129 (2014).

[17] R. Comin *et al.* Science **343** 390 (2013).

[18] M. Grilli and B. G. Kotliar, Phys. Rev. Lett. **64**, 1170 (1990)

[19] Z. Wang, G. Kotliar, and X.-F. Wang, Phys. Rev. B **42**, 8690 (1990).

[20] A. Georges, G. Kotliar, W. Krauth, and M. Rozenberg, Rev. Mod. Phys. **68**, 13 (1996).

[21] R. Bulla, T. Costi, and T. Pruschke, Rev. Mod. Phys. **80**, 395 (2008).

[22] J. Graf, G.-H. Gweon, K. McElroy, S. Y. Zhou, C. Jozwiak, E. Rotenberg, A. Bill, T. Sasagawa,

H. Eisaki, S. Uchida, H. Takagi, D.-H. Lee, and A. Lanzara, Phys. Rev. Lett. **98**, 067004 (2007).

[23] A. Macridin, M. Jarrell, T. Maier, and D. J. Scalapino, Phys. Rev. Lett. **99**, 237001 (2007).

[24] R. Žitko, D. Hansen, E. Perepelitsky, J. Mravlje, A. Georges, and B. S. Shastry, Phys. Rev. B **88**, 235132 (2013).

[25] H. Meier, C. Pépin, M. Einenkel, and K. B. Efetov, arXiv:1312.2010.

[26] D. Chowdhury and S. Sachdev, to appear.

[27] R. Comin *et al.*, arXiv:1402.5415.

[28] K. Fujita *et al.*, arXiv:1404.0362.